Nanoscale

PAPER

View Article Online
View Journal

Cite this: DOI: 10.1039/d5nr04317d

The supramolecular architecture of amyloid fibrils formed by a human tau-derived hexapeptide VQIVYK

Irene del Mar Fariñas Lucas,†[a,c] Youssra K. Al-Hilaly, †[a,b] Liisa Lutter,*[c] Wei-Feng Xue *[c] and Louise C. Serpell *[a]

The sequence $_{306}$VQIVYK$_{311}$ is an aggregation-prone region of the tau protein implicated in driving the assembly of tau into paired helical filaments. These filaments accumulate as intraneuronal neurofibrillary tangles in Alzheimer's disease and a range of tauopathies. Prolonged incubation of VQIVYK results in highly ordered fibrillar structures that give rise to unusually detailed and highly oriented X-ray fibre diffraction patterns. These mature fibrils provided the opportunity to use a novel integrative approach that combined X-ray fibre diffraction analysis with 3D contact point reconstruction atomic force microscopy (CPR-AFM) of individual filaments to determine molecular and supramolecular details. X-ray diffraction analysis resulted in a molecular model consistent with an X-ray crystallography structure, which could be further optimised to give rise to a highly twisted filamentous protofilament architecture. Analysis of individual fibril envelopes by CPR-AFM revealed a diverse polymorphous population with a major fibril morphology of apparently smooth, cylindrical fibrils, and morphological subpopulations of fibrils with clear left-handed twisting patterns, while X-ray diffraction suggests that the protofilament core structure remains consistent between the polymorphs. Here, we reveal that VQIVYK amyloid fibrils form a polymorphous amyloid population by assembly of highly ordered protofilaments. The combined approach provides novel molecular and supramolecular information regarding the structure of highly twisted amyloid fibrils.

Received 13th October 2025,
Accepted 22nd December 2025

DOI: 10.1039/d5nr04317d

rsc.li/nanoscale

Introduction

Amyloid fibrils are defined by the organisation of β-strands that run perpendicular to the fibre axis and are hydrogen bonded along the length of the fibre axis to generate a highly ordered architecture.[1] The β-sheets are associated *via* interdigitation of the amino side chains to result in a molecular structure with high stability and impressive tensile strength.[2–4] Amyloid fibrils are well known for their association with protein misfolding diseases,[5,6] which include neurodegenerative diseases like Alzheimer's disease[7] and systemic amyloidoses such as Senile Systemic Amyloidosis.[8] Functional amyloid fibrils provide adhesion and protection in many organisms, such as curli in certain bacteria[9] and PMel17 in human melanosomes.[10] They can also play an important role in controlling memory[11] and in viral infection.[12] Due to their inherent strength, amyloid fibrils have been developed as functional materials in a number of bionanomaterial applications.[13–15]

Tau is an amyloidogenic protein that self-assembles to form paired helical filaments (PHFs) that are found intracellularly in the neurons of Alzheimer's brain tissue.[16] PHFs are amyloid structures that display all the defining characteristics of a cross-β structure.[17] Full-length tau is mostly an intrinsically disordered protein, but several regions of tau have been identified that may serve to drive self-assembly to form fibrils. These are hexapeptide sequences named PHF6 and PHF6* and have the sequences VQIVYK and VQIINK.[18–20] These hexapeptide fibrils are not found physiologically. The crystal structures of VQIVYK fibrillar microcrystals show the classical cross-β structure within a 3D lattice[19] with a steric zipper architecture similar to fibrous crystals formed by other short amyloidogenic peptides.[3,19] Cryo-electron microscopy (cryo-EM) has provided a 3D structure for the tau paired helical filament (PHF) from Alzheimer's disease brain. Here, the core filament-forming region extends from tau 304 to 380 with a parallel β-sheet organisation where each peptide is stacked above an

[a]Sussex Neuroscience, School of Life Sciences, University of Sussex, Falmer, BN1 9QG E. Sussex, UK. E-mail: L.C.Serpell@sussex.ac.uk
[b]Chemistry Department, College of Science, Mustansiriyah University, Baghdad, Iraq
[c]School of Biosciences, University of Kent, Canterbury CT2 7NJ, UK.
E-mail: W.f.Xue@kent.ac.uk
† Equal authors.

identical sequence.[21] The hexapeptide $_{306}$VQIVYK$_{311}$ is found in a β-strand that pairs across the sheet and interdigitates with a peptide $_{378}$FTLKHT$_{373}$ across an antiparallel zipper in *ex vivo* fibril structures extracted from tissues of patients with both Alzheimer's disease and chronic traumatic encephalopathy.[22,23] In *ex vivo* structures from corticobasal degeneration brain tissue, VQIVYK forms part of the central four-layered cross-β packing,[24] but in all tauopathy filament structures, the sequence is arranged in a parallel β-sheet. These structures point to an important role of the VQIVYK region. Understanding its propensity to form amyloid fibrils alone may provide insight into the parallel stacking arrangement of a range of disease-relevant tau fibril structures and their potential for polymorphic assembly. Structure determination from PHFs formed from tau 297–391 *in vitro* has shown that the structures mature with incubation time,[25] providing further insights into the importance of structural polymorphism with fibril maturation and disease progression.

X-ray crystallography from microcrystals and Cryo-EM from *ex vivo* and *in vitro* fibrils has provided useful structural details of amyloid organisation. However, these techniques have not been able to provide longer-range, supramolecular details due to reliance on the cross-β repeat as well as averaging over many molecules. Here, we have combined X-ray fibre diffraction with *individual filament* atomic force microscopy and gone beyond the cross-β repeat to provide a model for the full fibrillar structure of the VQIVYK fibril. VQIVYK has been widely observed to form amyloid fibrils spontaneously in aqueous buffer and water.[26] Previous work has shown that short peptides (*e.g.* GNNQQNY and HYFNIF sequences) and longer proteins (tau 297–391) are able to form fibrils that mature with time.[25,27,28] We report that following prolonged incubation, VQIVYK forms exceptionally well-ordered amyloid fibrils, giving rise to an unusually detailed X-ray fibre diffraction pattern that is not typically seen for amyloid fibril samples. AFM reveals a polymorphic population, dominated by a smooth filament morphology without detectable twist, and subpopulations with left-handed twisted fibrils. The exceptionally detailed X-ray fibre diffraction patterns were analysed alongside complementary atomic force microscopy imaging data with individual filament structural analysis by 3D contact point reconstruction (CPR-AFM). The integrated approach generated a supramolecular model of the filament structure that describes both the commonality and the individuality of VQIVYK fibrils and suggests lateral assembly of protofilaments into fibrils as a source of structural polymorphism.

Materials and methods

Amyloid fibril formation

Ac-VQIVYK-NH_2 was purchased from JPT at 97% purity as a trichloroacetic acid salt. The peptide was dissolved in Milli-Q 0.22 μm filtered water at 1 mg ml^{-1} and was allowed to self-assemble at room temperature over two years. Samples were collected immediately (0 h), after 7 days incubation and after approximately two years.

Transmission electron microscopy

4 μL of fibril solution was applied to formvar-coated 400 mesh copper grids (Agar Scientific) and allowed to adhere for 60 seconds before blotting, washing with 4 μL of filtered Milli-Q distilled water and then incubating with 0.22 μm filtered uranyl acetate (2% w/v) for 30 seconds and then washed twice with 4 μL of filtered Milli-Q distilled water and allowed to air dry. The grids were examined using a JEOL JEM1400-Plus Transmission Electron Microscope (TEM) operated at 120 kV and images were collected at 20–40k magnification using a Gatan OneView camera (4k × 4k). Images were recorded at 25 fps with drift correction using DigitalMicrograph (GMS3, Gatan).

Atomic force microscopy data collection and analysis

The pre-assembled fibril sample was diluted 1/50 in sterile filtered Milli-Q water adjusted to pH 2.0 using a dilute solution of HCl. Immediately after dilution, 20 μL samples were deposited onto freshly cleaved mica surfaces (Agar Scientific, F7013) and incubated for 10 min. Following incubation, the sample was washed with 1 mL of the filter-sterilised HCl solution and dried using a stream of nitrogen gas. Fibrils were imaged using a Multimode 8 AFM with a Nanoscope V (Bruker) controller operating under peak-force tapping in the ScanAsyst mode using Bruker ScanAsyst probes (silicon nitride triangular cantilever with a nominal tip radius of 2 nm and a nominal spring constant of 0.4 N m^{-1}, Bruker). Height channel images, with scan sizes of 3 × 3 μm, 5 × 5 μm, or 8 × 8 μm, were collected with 2048 × 2048 pixels each. Nanoscope analysis software (Version 1.5, Bruker) was used to process the image data by flattening the height topology maps to remove tilt and scanner bow. Flattened image data were imported into Trace_y software,[29] where all subsequent analysis was carried out. Fibrils were traced and digitally straightened and the height profile for each fibril was extracted from the centre contour line of the straightened fibrils. A total of 61 individual filaments traced from 16 independently scanned images were analysed. The straightened fibril traces were corrected for the tip-convolution effect using an algorithm based on geometric modelling of the tip-fibril contact points, followed by 3D reconstruction of the fibril envelopes as previously described.[29] The method involves determining the helical pitch of each fibril through Fourier transformation of the fibril centre contour heights. Where this was not possible due to lack of any clear periodicity in the central line height profile of the fibril, the mean pitch of fibrils with detectable pitch was used. Out of the 61 fibrils analysed, 51 fibrils have a smooth cylindrical appearance, and their mean cross-sectional area estimated following correction of the tip–sample convolution effect (example shown in SI Fig. S1) was 64.5 ± 3.4 nm^2 (mean ± sd). It was previously confirmed on these smooth fibrils that while varying the pitch from 10 to 100 pixels the mean difference between the maximum and minimum of mean cross-sec-

tional area values is 0.23 nm^2, indicating that using an average pitch in the case of these smooth fibrils has comparatively little effect on the cross-sectional area measurements from the reconstructed fibril envelope models.

X-ray fibre diffraction data collection and analysis

A 10 μL droplet was placed between two wax-tipped capillary tubes arranged in a Petri dish at 4 °C and allowed to dry for several days. The resulting bundle of fibrils on a capillary tube was mounted on a goniometer head, and X-ray fibre diffraction data were collected using a Rigaku CuKα rotating anode and an RAxis 4++ detector. Exposure times were 30 s or 60 s with a specimen to detector distance of 50 or 100 mm, respectively. Patterns were converted to tiff format and inspected using CLEARER.[30] The patterns were *centred* and radially averaged, and the diffraction signal positions were measured using the *peak finder* tool in CLEARER. The signal positions were further confirmed using the *Zoom and Measure* tool. Values that diverged from the equatorial were measured using the angle in pixels from the origin and calculated using trigonometry. Unit cell dimensions were derived using the *unit cell determination* tool following the input of equatorial diffraction signals.

Modelling

Models were prepared using the X-ray crystallography structure 2ON9.pdb[19] as a starting model. A model structure was generated using a Python script that imposes specific translation and rotation parameters, and these models were generated using Pymol (Schrödinger, LLC., USA).

Diffraction pattern calculation

Diffraction patterns were calculated from PDB coordinates generated from Pymol using the *Diffraction simulation tool* in CLEARER and the determined unit cell parameters.[30]

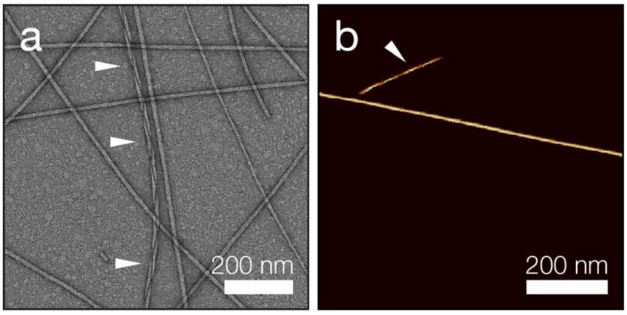

Fig. 1 Micrographs showing amyloid fibrils formed by VQIVYK following prolonged incubation. (a) TEM shows a major population of smooth fibrils and fewer with a pronounced twist. (b) AFM shows very long smooth fibrils and a smaller population of twisted fibrils made up of protofilaments. White arrows highlight twisted fibrils in (a) and (b).

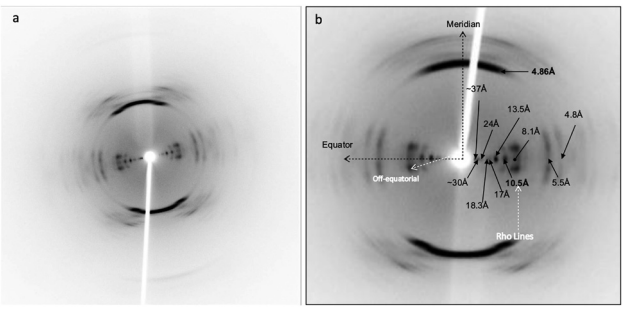

Fig. 2 X-ray fibre diffraction from amyloid fibrils formed by VQIVYK. (a) Diffraction pattern taken with a distance of 50 mm. (b) Diffraction pattern taken at a 100 mm specimen-to-detector distance. Diffraction signals are labelled and the characteristic cross-β signals on the meridian (4.76 Å) and equator (10.5 Å) are highlighted in bold. Additional equatorial signals are observed at 10.5 Å, 5.5 Å and 4.8 Å, with lower angle signals labelled. From the equatorial signal at 10.5 Å, a low intensity-split pattern arises, while 8.1 Å displays a split pattern with higher intensity than the signal at the equator. The equator and meridian are labelled with black dotted lines and the off-equatorial and rho line directions are shown in white dotted lines.

Results

X-ray fibre diffraction reveals semi-crystalline order within VQIVYK protofilaments

Transmission electron microscopy and atomic force microscopy revealed a very straight, mostly smooth appearance of the fibrils arising from extended incubation of VQIVYK (Fig. 1). X-ray fibre diffraction patterns were collected from the partially aligned VQIVYK fibrils. These showed a classical cross-β diffraction pattern with the expected 4.86 Å and 10.5 Å diffraction signals perpendicular to one another on the meridian and equator, respectively. These signals arise from hydrogen-bonded β-strands, and from the β-sheet spacing, the chain length and the protofilament packing[31] (Fig. 2). Remarkably, the detailed diffraction pattern showed that the fibrils within the fibre sample were extremely well oriented and semi-crystalline (Fig. 2 and Table 1). TEM of fibrils formed immediately (0 h) and at 7 days shows less mature, more twisted fibrils, and the cross-β pattern lacks the finer detail of the pattern collected following prolonged incubation (Fig. S2). Extended incubation samples showed diffraction signals observed at 8.3 Å and 10.5 Å with a split appearance as off-equatorial or rho lines (Fig. 2 and Fig. S3), which were not apparent for the less mature fibril pattern.

The X-ray crystallography structure of the VQIVYK peptide has been solved from microcrystals,[19] with unit cell dimensions determined as a = 4.86 Å, b = 61.93 Å, c = 15.41 Å; α = 90.00°, β = 98.11°, γ = 90.00°. The unit cell contains two peptides arranged with the same side chains facing each other in a "face-to-face" configuration (2ON9.pdb) (Fig. 3a and b). An X-ray fibre diffraction pattern was calculated using the crystal structure coordinates and unit cell dimensions submitted with 2ON9.pdb. The calculated pattern showed a good match with the experimental diffraction pattern from VQIVYK fibrils (Fig. 3) (Table 1). However, the structure solved from 3D microcrystals necessarily does not incorporate a twist in the

Table 1 Diffraction signal positions from the experimental fibre diffraction pattern from the VQIVYK fibril sample compared to the fibre diffraction signals calculated from 2ON9.pdb and the twisted model structure in the cell with a = 4.86 Å, b = 61.93 Å, c = 15.41 Å; α = 90.00°, β = 98.11°, γ = 90.00°

Experimental diffraction signals from VQIVYK fibrils (Å)	Calculated signals from 2ON9.pdb	Calculated from the model
Equatorials		
~37		
~30	30.94	30
24		
18.3	18.52	18.52
17		
	16.2	
13.5	14.1	13.11
10.5	10.74	10.22
8.1	8.54	8.54
	6.15	6.15
5.5	5.44	5.61
4.8	4.99	4.9
Meridionals		
4.8	4.8	4.8

β-strands, and the calculated pattern does not give rise to the observed split in the equatorial signals, implying that some detail is missing in the model structure.

Measurement of the angle of the split reflections from the equator is 27.70° (Fig. S2), and this twist was incorporated into the model structure as a twist of 13.85° for each of the strands within each sheet. This gives a helical pitch of approximately 124 Å for 26 stacked peptides, resulting in a highly twisted filament (Fig. 3). Calculation of the diffraction pattern from this twisted model structure gives rise to a good match between the calculated and experimental diffraction data (Table 1) and helps to validate the model. Although there are close similarities between the experimental and calculated data, we cannot rule out the possibility that another model may also fit the data. This is a model of the protofilament.

The unit cell from the VQIVYK crystal was further optimised to accommodate the twist and has been updated to a = 4.86 Å, $b \approx 58$ Å(2), $c \approx 18$ Å; α = 90.00°, β = 98.11°, γ = 90.00°. The twisting architecture results in new interactions in the hydrogen bonding of the inter-sheet plane (Fig. 4). The side chains from upper layers bond with lower layers, forming a very stable conformation. As a result, Tyr is closer to the adjacent β-strand than in the planar conformation of the crystal, and aromatic residues make a strong contribution to steric zipper stability.[15]

Structural analysis of individual fibrils by atomic force microscopy shows a mixture of fibril structures within the VQIVYK fibril population

X-ray fibre diffraction provides short-range information on the core structures of fibrous architecture, while electron microscopy revealed their polymorphic supramolecular organisation. AFM analysis was subsequently employed to investigate the polymorph distribution by individual filament structural analysis. Tracing of 61 individual fibrils from AFM images revealed a major fibril population with an apparently smooth cylindrical envelope. This is consistent with highly twisted fibrils where the helical pitch is on the order of 12 nm, as suggested by the XRFD data. Smooth fibrils have a consistent mean height in the range of 8.6 nm to 9.6 nm (Fig. 5), suggesting that the fibrils are formed from multiple protofilaments with the ordered core structure seen in the XRFD analysis. Sub-populations of observably twisted fibrils with a clearer pattern of peaks and troughs across the central line height profile compared with the smooth fibrils were also observed with a comparatively larger range of mean height values below that of the major population between 5.7 nm and 9.2 nm, and a large degree of variation in twist and morphology. These sub-populations of fibrils may represent species that were not fully assembled compared with the major population of mature fibrils. The handedness of the helical twist of all fibrils in this population was left-handed,

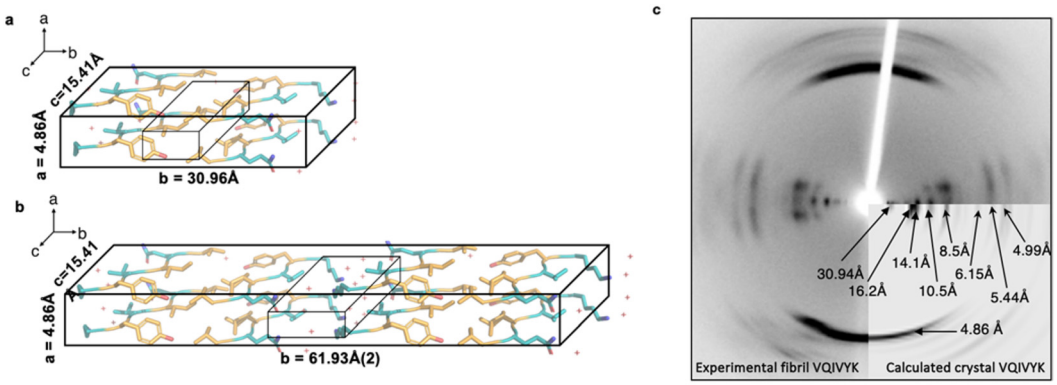

Fig. 3 The structure of fibrillar VQIVYK. (a) The 2ON9.pdb structure is shown in the unit cell derived from the crystal structure.[19] Peptide association depicts the inter-sheet hydrogen bonds between side chains (shown in orange) in a dry steric zipper, highlighted by the smaller box. (b) Full unit cell with four peptides along the **b** lattice vector. Red crosses represent the water molecules that H-bond with blue side chains in the wet steric zipper. The figure was prepared using Pymol. (c) Experimental XRDP from fibrillar VQIVYK compared with the pattern calculated from the 2ON9.pdb 3D model using the unit cell derived from the crystal structure 2ON9.pdb (a = 4.86 Å, b = 61.93 Å, c = 15.41 Å; α = 90.00°, β = 98.11°, γ = 90.00°).[19]

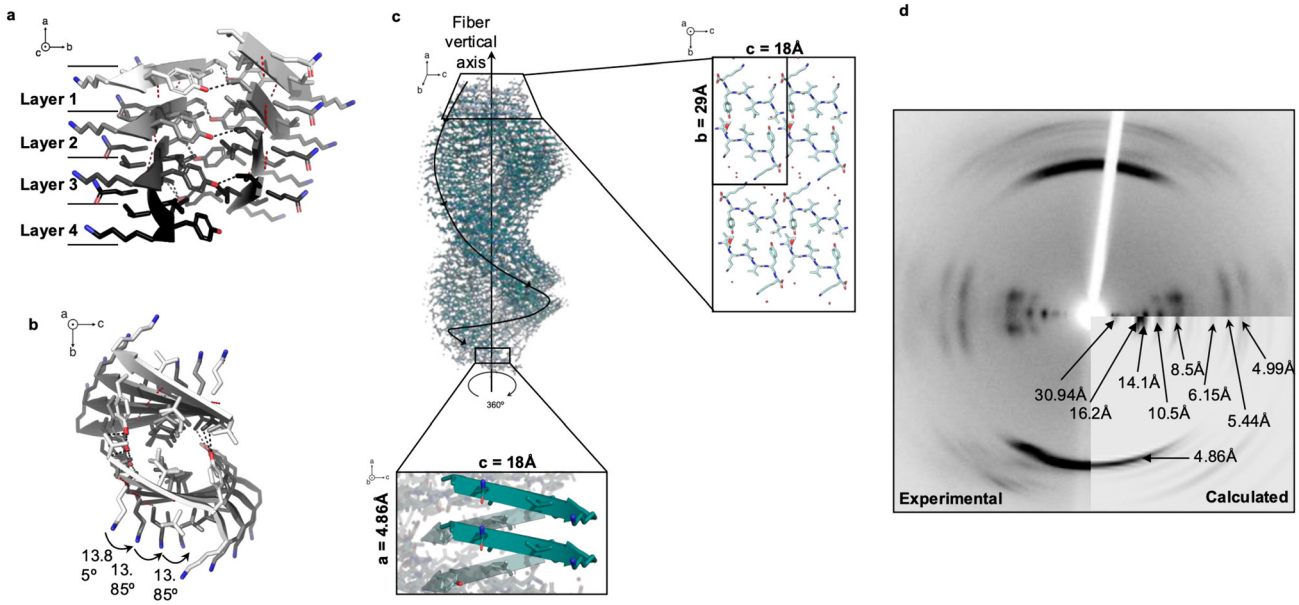

Fig. 4 Molecular model of VQIVYK fibrils. (a) The twist between parallel β-strands allows hydrogen bonding (red dashed line) in the lattice vector **a** (4.86 Å) forming β-sheets. In the horizontal axes, interactions link side chains from upper layers with lower ones, forming very stable hydrogen bonding (black dashed line) in the **b** lattice vector and maintains the intra-sheet bonding distance of 4.86 Å. The layers interact *via* inter-bonding between layers 1–2, 2–3 and 3–4. (b) Perspective parallel to the fibre axis (**a** lattice vector) showing the angle applied to the equator of the protofilament. (c) The 3D molecular structure of the protofilament shows the twist of 13.85° from layer to layer. The rotation is applied in the equator, resulting in 26 monomers per repeat. (d) The comparison between the calculated pattern from the model created using 2ON9.pdb with an additional 27° twist and the experimental data. The optimised model provides an additional diffraction signal that matches with the reflection at 18 Å and split off-meridians that simulate the experimental pattern.

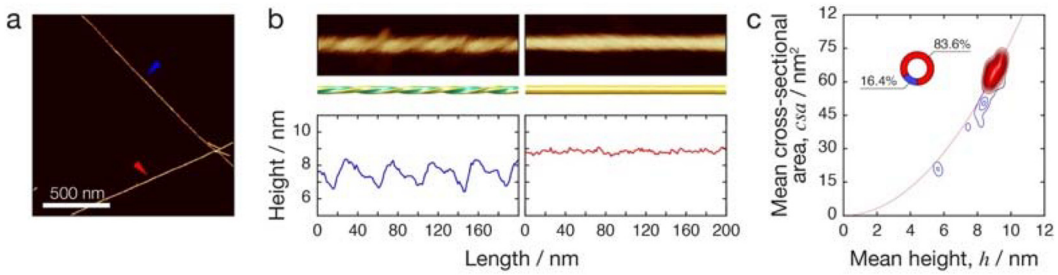

Fig. 5 AFM analysis of VQIVYK fibrils shows a major morphology of smooth and cylindrical fibrils and a minor sub-population of fibrils with various twisting morphologies. (a) AFM image of VQIVYK fibrils. Scale bar represents 500 nm. (b) Analysis of two fibrils with different morphologies. The fibrils shown in (b) are those highlighted with blue and red arrows in (a), respectively. The top panels show straightened AFM images of a 200 nm section of the fibrils. The middle panels show reconstructed 3D envelopes of the fibrils. The bottom panels show the height profiles of the fibrils across the central lines of the straightened filaments. A 200 nm segment along the length of the reconstructed fibrils is shown for comparison. (c) Mean height of the fibril central line plotted against the mean cross-sectional area estimated by 3D contact point reconstruction AFM. Distribution densities from 61 individual fibrils are plotted. The smooth fibrils are shown in red and fibrils with a clear peak-and-trough pattern are shown in blue. The inset shows the relative size of the two sub-populations. The black lines show values expected for perfectly cylindrical fibrils.

inferring that the handedness for the major population of smooth cylindrical fibrils is likely to be left-hand twisted.

Integrating structural information from XRFD and AFM allowed creation of multi-scale structural models of VQIVYK fibrils

Reconstruction of three-dimensional envelopes from traced and straightened fibril height data enabled the average cross-sectional area to be calculated for each individual fibril. Here, we explored whether it is possible to estimate the number of pairs of VQIVYK β-sheets that pack laterally to form the fibril ultrastructure. Simple comparison of areas between the half-unit cell of paired β-sheets and cross-sections of the smooth fibrils suggests that this contains between 11 and 14 peptide pairs that could be packed to form smooth fibrillar cross-sections (Fig. 6). A different arrangement with a more elongated cross-sectional shape would be expected for the minor, visibly twisted fibril populations. Intrafibrillar variation in the

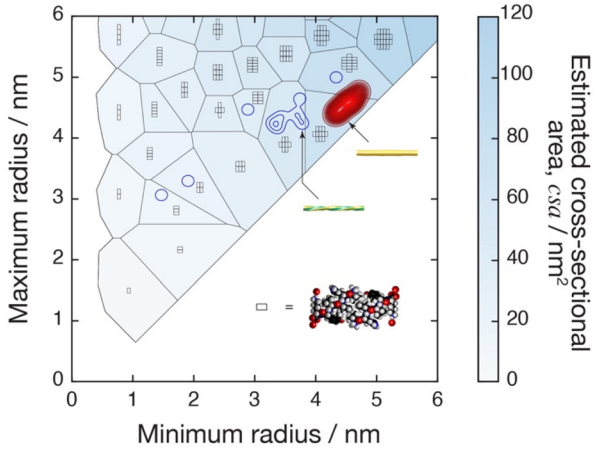

Fig. 6 Possible packing arrangements of VQIVYK unit cell cross-sections. Arrangements of pairs of VQIVYK β-sheets in a half-unit cell modelled from the XRFD (symbolised by the rectangles) mapped onto the cross-sectional dimensions of fibril envelopes reconstructed from the AFM data. The possible packing arrangements tested are those with fully convex cross-sections and two-fold symmetry. Regions consistent with each of the arrangements are shown with an illustration of the packing of the peptide pairs (rectangles), and the colour of the regions indicate the cross-sectional area estimated by the cross-sections' convex hull area. This is mapped onto the polymorph distribution of the fibrils visualised by their minimum radius plotted against the maximum radius obtained by 3D CPR-AFM. The distribution of smooth fibrils is shown in red and the distribution of fibrils with a clear peak-and-trough pattern is shown in blue.

number of peptide pairs or their arrangement could be used to explain the morphology of the fibrils, as shown in Fig. 6.

Conclusions

Major advances have been made to understand the architecture of amyloid fibrils[1,32] from microcrystallography and cryo-electron microscopy, both providing exciting details regarding the interactions between side chains in steric zippers and the organisation of in-register parallel stacking of individual protein chains. However, the limitations of these techniques due to bulk averaging and reliance on the cross-β repeat mean that supramolecular structures are undefined. X-ray crystallography utilising microcrystals of amyloid-forming peptides has generated structures showing peptides within a crystalline lattice and revealed the steric zipper arrangement.[3] Cryo-EM analysis of fibrillar structures uses a single-particle averaged approach with a rise of 4.75 Å alongside the classification of cross-over repeat distances.[33] Both cryo-EM and X-ray crystallography analyses require averaging over numerous molecules. X-ray fibre diffraction provides details of repeating units within the fibrils and can also provide information regarding the helical twist. The amount of information regarding the structural model relies on the detail within the diffraction pattern, which in turn arises from the order within the fibril sample. CPR-AFM is used here to provide high-resolution details of the molecular envelope and has been developed to enable detailed reconstruction from individual fibrils.

Here, using a powerful combination of X-ray fibre diffraction to define the molecular architecture of the protofilament cores in the sample, and atomic force microscopy to provide details of the molecular envelope for each individual filament, we have gained valuable insights into the overall assembly and organisation of peptides within an amyloid fibril and concluded that the fibrils are assembled from protofilament building blocks with highly ordered and common cores. We show that a fine twist within the sheets creates a tight helix which results in very ordered fibril cores. This provides useful data regarding the physics of filament twist that often define the precise amyloid polymorph structures.[34,35] The atomic force microscopy analysis supports the structural model. Furthermore, we show, from this prolonged incubation of an amyloidogenic peptide, that this can converge to form extremely stable, ordered fibril core structures. Here, we have described a supramolecular structure of a fibril formed by a hexapeptide following prolonged incubation. While this model system has little direct physiological relevance, we have demonstrated advances in structure determination of the longer-range architecture from our combined approach which can be used for disease relevant structures in the future.

Author contributions

Irene del Mar Farinas Lucas and Louise Serpell: writing – original draft. Irene del Mar Farinas Lucas, Youssra Al-Hilaly, and Liisa Lutter: investigation, data acquisition, formal analysis and validation. Louise Serpell and Wei-Feng Xue: supervision and funding acquisition. Wei-Feng Xue: software. Youssra Al-Hilaly, Irene del Mar Farinas Lucas, Liisa Lutter, Louise Serpell, and Wei-Feng Xue: visualisation, writing and editing.

Conflicts of interest

There are no conflicts to declare.

Data availability

The data supporting this article have been included as part of the supplementary information (SI). Supplementary information: Fig. S1. AFM tip convolution effect. Fig. S2. X-ray fibre diffraction and TEM from 0 and 7 day incubated VQIVYK. Fig. S3. Close up view of the equatorial region of the diffraction pattern. See DOI: https://doi.org/10.1039/d5nr04317d.

Acknowledgements

YA wishes to thank the Ministry of Higher Education and Scientific Research of Iraq for the support and funding. This work was supported by funding from the Biotechnology and

Biological Sciences Research Council (BBSRC), UK grant BB/S003657/1, BB/S003312/1 and BB/Z516880/1, and Engineering and Physical Sciences Research Council (EPSRC), UK DTP grant EP/R513246/1 (LL).

References

1 M. Sunde, L. Serpell, M. Bartlam, P. Fraser, M. Pepys and C. Blake, *J. Mol. Biol.*, 1997, **273**, 729–739.
2 T. P. Knowles, A. W. Fitzpatrick, S. Meehan, H. R. Mott, M. Vendruscolo, C. M. Dobson and M. E. Welland, *Science*, 2007, **318**, 1900–1903.
3 D. S. Eisenberg and M. R. Sawaya, *Annu. Rev. Biochem.*, 2017, **86**, 69–95.
4 O. S. Makin, E. Atkins, P. Sikorski, J. Johansson and L. C. Serpell, *Proc. Natl. Acad. Sci. U. S. A.*, 2005, **102**, 315–320.
5 J. D. Sipe, M. D. Benson, J. N. Buxbaum, S. Ikeda, G. Merlini, M. J. Saraiva and P. Westermark, *Amyloid*, 2014, **21**, 221–224.
6 C. M. Dobson, T. P. J. Knowles and M. Vendruscolo, *Cold Spring Harbor Perspect. Biol.*, 2020, 12.
7 G. B. Irvine, O. M. El-Agnaf, G. M. Shankar and D. M. Walsh, *Mol. Med.*, 2008, **14**, 451–464.
8 J. D. Sipe, *Annu. Rev. Biochem.*, 1992, **61**, 947–975.
9 M. R. Chapman, L. S. Robinson, J. S. Pinkner, R. Roth, J. Heuser, M. Hammar, S. Normark and S. J. Hultgren, *Science*, 2002, **295**, 851–855.
10 D. M. Fowler, A. V. Koulov, W. E. Balch and J. W. Kelly, *Trends Biochem. Sci.*, 2007, **32**, 217–224.
11 R. Hervas, M. J. Rau, Y. Park, W. Zhang, A. G. Murzin, J. A. J. Fitzpatrick, S. H. W. Scheres and K. Si, *Science*, 2020, **367**, 1230–1234.
12 P. Léger, E. Nachman, K. Richter, C. Tamietti, J. Koch, R. Burk, S. Kummer, Q. Xin, M. Stanifer, M. Bouloy, S. Boulant, H.-G. Kräusslich, X. Montagutelli, M. Flamand, C. Nussbaum-Krammer and P.-Y. Lozach, *Nat. Commun.*, 2020, **11**, 3281.
13 Z. S. Al-Garawi, G. E. Kostakis and L. C. Serpell, *J. Nanobiotechnol.*, 2016, **14**, 79.
14 S. Mankar, A. Anoop, S. Sen and S. K. Maji, *Nano Rev.*, 2011, **2**, 6032.
15 S. L. Gras, in *Advances in Chemical Engineering*, ed. R. J. Koopmans, Academic Press, 2009, vol. 35, pp. 161–209.
16 M. Goedert, *Ann. N. Y. Acad. Sci.*, 1996, **777**, 121–131.
17 J. Berriman, L. C. Serpell, K. A. Oberg, A. L. Fink, M. Goedert and R. A. Crowther, *Proc. Natl. Acad. Sci. U. S. A.*, 2003, **100**, 9034–9038.
18 S. Maurer-Stroh, M. Debulpaep, N. Kuemmerer, M. L. de la Paz, I. C. Martins, J. Reumers, K. L. Morris, A. Copland, L. Serpell, L. Serrano, J. W. Schymkowitz and F. Rousseau, *Nat. Methods*, 2010, **7**, 237–242.
19 M. R. Sawaya, S. Sambashivan, R. Nelson, M. I. Ivanova, S. A. Sievers, M. I. Apostol, M. J. Thompson, M. Balbirnie, J. J. Wiltzius, H. T. McFarlane, A. O. Madsen, C. Riekel and D. Eisenberg, *Nature*, 2007, **447**, 453–457.
20 H. Inouye, D. Sharma, W. J. Goux and D. A. Kirschner, *Biophys. J.*, 2006, **90**, 1774–1789.
21 B. Falcon, W. Zhang, M. Schweighauser, A. G. Murzin, R. Vidal, H. J. Garringer, B. Ghetti, S. H. W. Scheres and M. Goedert, *Acta Neuropathol.*, 2018, **136**, 699–708.
22 B. Falcon, J. Zivanov, W. Zhang, A. G. Murzin, H. J. Garringer, R. Vidal, R. A. Crowther, K. L. Newell, B. Ghetti, M. Goedert and S. H. W. Scheres, *Nature*, 2019, **568**, 420–423.
23 S. S. Oakley, M. B. Maina, K. E. Marshall, Y. K. Al-Hilaly, C. R. Harrington, C. M. Wischik and L. C. Serpell, *Front. Neurol.*, 2020, **11**, 590754.
24 S. H. Scheres, W. Zhang, B. Falcon and M. Goedert, *Curr. Opin. Struct. Biol.*, 2020, **64**, 17–25.
25 S. Lövestam, F. A. Koh, B. van Knippenberg, A. Kotecha, A. G. Murzin, M. Goedert and S. H. W. Scheres, *eLife*, 2022, **11**, e76494.
26 W. J. Goux, L. Kopplin, A. D. Nguyen, K. Leak, M. Rutkofsky, V. D. Shanmuganandam, D. Sharma, H. Inouye and D. A. Kirschner, *J. Biol. Chem.*, 2004, **279**, 26868–26875.
27 K. L. Morris, A. Rodger, M. R. Hicks, M. Debulpaep, J. Schymkowitz, F. Rousseau and L. C. Serpell, *Biochem. J.*, 2013, **450**, 275–283.
28 K. E. Marshall, M. R. Hicks, T. L. Williams, S. V. Hoffmann, A. Rodger, T. R. Dafforn and L. C. Serpell, *Biophys. J.*, 2010, **98**, 330–338.
29 W. F. Xue, *Structure*, 2025, **33**, 363–371.
30 O. S. Makin, P. Sikorski and L. C. Serpell, *Appl. Crystallogr.*, 2007, **40**, 966–972.
31 O. S. Makin and L. C. Serpell, *FEBS J.*, 2005, **272**, 5950–5961.
32 A. J. Geddes, K. D. Parker, E. D. Atkins and E. Beighton, *J. Mol. Biol.*, 1968, **32**, 343–358.
33 S. Lovestam and S. H. W. Scheres, *Faraday Discuss.*, 2022, 240–243.
34 J. Adamcik and R. Mezzenga, *Soft Matter*, 2011, **7**, 5437–5443.
35 X. Periole, T. Huber, A. Bonito-Oliva, K. C. Aberg, P. C. A. van der Wel, T. P. Sakmar and S. J. Marrink, *J. Phys. Chem. B*, 2018, **122**, 1081–1091.